PAPER

Controlling Cu–Sn mixing so as to enable higher critical current densities in RRP$^{®}$ Nb$_3$Sn wires

To cite this article: Charlie Sanabria *et al* 2018 *Supercond. Sci. Technol.* **31** 064001

View the article online for updates and enhancements.

Controlling Cu–Sn mixing so as to enable higher critical current densities in RRP® Nb₃Sn wires

Charlie Sanabria[1,3] ⬤**, Michael Field**[2]**, Peter J Lee**[1] ⬤**, Hanping Miao**[2]**, Jeff Parrell**[2] **and David C Larbalestier**[1]

[1] Applied Superconductivity Center, NHMFL, Florida State University, 2031 E Paul Dirac Drive, Tallahassee, FL 32310, United States of America
[2] Bruker OST, 600 Milik Street, Carteret, NJ, 07008, United States of America
[3] Now at: Lawrence Berkeley National Laboratory, 1 Cyclotron Road, Berkeley, CA 94720-8201, United States of America

E-mail: csanabria@lbl.gov

Abstract

Dipole magnets for the proposed Future Circular Collider (FCC) demand specifications significantly beyond the limits of all existing Nb₃Sn wires, in particular a critical current density (J_c) of more than 1500 A mm^{-2} at 16 T and 4.2 K with an effective filament diameter (D_{eff}) of less than 20 μm. The restacked-rod-process (RRP®) is the technology closest to meeting these demands, with a J_c (16 T) of up to 1400 A mm^{-2}, residual resistivity ratio > 100, for a sub-element size D_s of 58 μm (which in RRP® wires is essentially the same as D_{eff}). An important present limitation of RRP® is that reducing the *sub-element size* degrades J_c to as low as 900 A mm^{-2} at 16 T for $D_s = 35$ μm. To gain an understanding of the sources of this J_c degradation, we have made a detailed study of the phase evolution during the Cu–Sn 'mixing' stages of the wire heat treatment that occur prior to Nb₃Sn formation. Using extensive microstructural quantification, we have identified the critical role that the Sn–Nb–Cu ternary phase (*Nausite*) can play. The Nausite forms as a well-defined ring between the Sn source and the Cu/Nb filament pack, and acts as an osmotic membrane in the 300 °C–400 °C range— greatly inhibiting Sn diffusion into the Cu/Nb filament pack while supporting a strong Cu counter-diffusion from the filament pack into the Sn core. This converts the Sn core into a mixture of the low melting point (408 °C) η phase (Cu₆Sn₅) and the more desirable ε phase (Cu₃Sn), which decomposes at 676 °C. After the mixing stages, when heated above 408 °C towards the Nb₃Sn reaction, any residual η liquefies to form additional irregular Nausite on the inside of the membrane. All Nausite decomposes into NbSn₂ on further heating, and ultimately transforms into coarse-grain (and often disconnected) Nb₃Sn which has little contribution to current transport. Understanding this critical Nausite reaction pathway has allowed us to simplify the mixing heat treatment to only one stage at 350 °C for 400 h which minimizes Nausite formation while encouraging the formation of the higher melting point ε phase through better Cu–Sn mixing. At a D_s of 41 μm, the Nausite control heat treatment increases the J_c at 16 T by 36%, reaching 1300 A mm^{-2} (i.e. 2980 A mm^{-2} at 12 T), and moving RRP® closer to the FCC targets.

Keywords: RRP wire heat treatment, Nb₃Sn wire heat treatment, critical current improvement, Nausite, accelerator magnets, Future Circular Collider, Hi-lumi upgrade

(Some figures may appear in colour only in the online journal)

1. Introduction

To advance experimental high energy physics beyond the Large Hadron Collider (LHC), a Future Circular Collider (FCC) [1, 2] has been proposed with a proton center-of-mass energy of 100 TeV and a circumference of about 100 km [3]. This is a major advance beyond the 14 TeV center-of-mass energy and 27 km circumference of the LHC [4], and it will require more than 5000 superconducting dipole magnets with magnetic fields of 16 T [5]—a demanding target compared to the 8 T magnets of the LHC [6]. This doubling of field requires a change from Nb–Ti to Nb$_3$Sn as the conductor technology. But the required properties, especially critical current densities (J_c) higher than 1500 A mm^{-2} at 16 T and an effective filament diameter (D_{eff}) of less than 20 μm [7], are well beyond the present state-of-the-art of Nb$_3$Sn. Furthermore, these properties must be retained while maintaining a residual resistivity ratio (RRR) of more than 150 and a piece length longer than 5 km [7].

Today, the production-grade Nb$_3$Sn wire which is closest to achieving such properties is the internal-tin restacked-rod-process (RRP®) wire, manufactured by the former Oxford Superconducting Technology (now Bruker OST since 2017). However, there is a strong J_c drop in RRP® wires once D_{eff} is reduced below $\sim$50 μm [8] for reasons that are still poorly understood. This paper directly addresses the causes of this drop and shows that J_c can be raised by redesigning the intermediate heat treatment stages to minimize Nb$_{0.75}$Cu$_{0.25}$Sn$_2$ ('Nausite') formation and maximize Cu diffusion into the core.

1.1. Basics of the RRP® design

RRP® Nb$_3$Sn wires, as the name implies, are comprised of a *stack* of 'sub-elements' that are themselves a product of a previous stacking sequence of Cu, Nb, and Sn rods. Sketches of a sub-element and a wire can be seen in figure 1, as well as a scanning electron image of a wire cross section. Because all the Nb filaments within a sub-element (Cu-clad Nb rods in figure 1(a)) bond together during the Nb$_3$Sn reaction to form a ring of Nb$_3$Sn, the physical diameter of the sub-element, D_s, is very close to the effective filament diameter, D_{eff}—a dimension that can be reduced by increasing the number sub-elements in a stack or by decreasing the wire diameter. Bruker OST has reached a very reliable 'mapping yield' [9] when restacking 108 sub-elements in a 127 *centered hexagonal number* placeholder configuration (127-stack), resulting in a D_s of 55 μm with a wire diameter of 0.85 mm. A slightly lower yield is obtained using a 169-stack, and higher stack counts (such as 217) are still experimental [8], but their development is necessary to eventually achieve D_{eff} dimensions required by the FCC specifications.

A standard 108/127 wire (at 0.85 mm in diameter, $D_s = 55$ μm) has an average J_c (16 T) of $\sim$1200 A mm^{-2}. This, however, as a result of the aforementioned J_c drop as a function of D_s, is lower than the previously reported record J_c (16 T) of 1350 A mm^{-2} achieved in an RRP® wire with a sub-

element size of 72 μm [10]. Discovering the root cause of this J_c degradation has been a key motivation for this study.

In the past decade, Bruker OST has also had significant success in optimizing the Cu/Nb/Sn metal ratios [11], the upper critical field (H_{c2}) dopant [12], and the fabrication reproducibility [10] of RRP® wires. One of the most recent successful modifications was a slight increase of the Nb:Sn atomic ratio [8] in the sub-element (from 3.4:1 to 3.6:1) in order to provide greater margin against Sn breaking through the diffusion barrier and degrading the RRR. Such a design change had a minor reduction in J_c while significantly improving RRR [12].

1.2. The RRP® heat treatment

Like all other internal-Sn wires, lower temperature heat treatments have been historically used in an attempt to mix the Cu and Sn prior to the Nb$_3$Sn reaction, in order to obtain a more homogenous Sn-rich phase around the Nb filaments and reduce the negative impact of liquid phases. It has previously been suggested that the multi-stage heat treatment of RRP® wires requires modifications to accommodate wire design changes [13]. However, only the final stage of this heat treatment ($\sim$650 °C) has been studied in RRP® with convincing enough evidence to alter the recommended heat treatment [14, 15]. In this article, we evaluate the impact that the mixing stages (below 600 °C) can have on wire performance.

Figure 2 shows the standard RRP® heat treatment with two Cu–Sn mixing stages at 215 °C and 400 °C, and one 'A15 reaction' at $\sim$665 °C. A cross section of a representative sub-element at the end of each isothermal heat treatment is also shown to illustrate the distribution of the phases. It is worth mentioning that the 215 °C is sometimes done at 210 °C [16], at 200 °C [17, 18], as well as 220 °C [19], depending on the type of wire. For simplicity, we will refer to this step as the 215 °C step in this paper.

Despite the extensive history of internal-Sn wires, there is considerable disagreement about the function and optimization of the mixing stages, which we explored in detail elsewhere [20]. Figure 3 shows the Cu–Sn phase diagram, which will be very relevant for the following section of this article since the main goal of the isothermal steps is to transform the Sn and Cu into the η and ε Cu–Sn phases (where the latter is preferable because of the low melting point of the former).

The original reasoning behind the early stages of the RRP® heat treatment was mainly to '*form the bronze phases and start the tin diffusion through the copper matrix*' and it is believed that if these steps are skipped the wires are '*subject to Sn bursting*' [16]. These so-called 'Sn bursts' destroyed several small magnets wound with MJR (Modified Jelly Roll) wires (a predecessor technology to RRP® which was subject to some mixing heat treatment studies [22–24]) made at the Applied Superconductivity Center in the early 1980s, and were assumed to be due to a pressure build-up during the liquefaction of pure Sn when heated continuously. It is important to mention that there are other reasons for using the
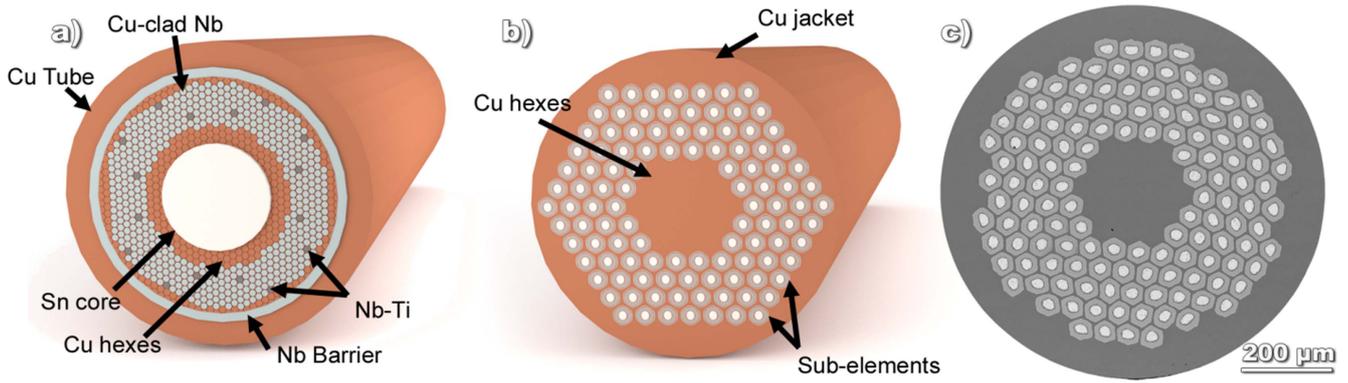
Figure 1. (a) A sketch of stacked Cu hexagons and Cu-clad Nb rods-in-hexagons, surrounded by a Nb barrier and a Cu tube. The Sn core is inserted into a gun-drilled hole after the Cu and Nb components have bonded. By interspersing Nb–Ti rods in the rod stack, shown in figure 1(a), the Nb$_3$Sn can be doped with Ti to increase the critical current density at high magnetic fields. (b) A sketch of a fully processed 108/127 RRP® wire after 108 sub-elements have been restacked with a core of 19 Cu hexes and a Cu jacket added. (c) A backscattered-electron micrograph of a 132/169 wire (three sub-elements on each corner have been removed in this particular design).
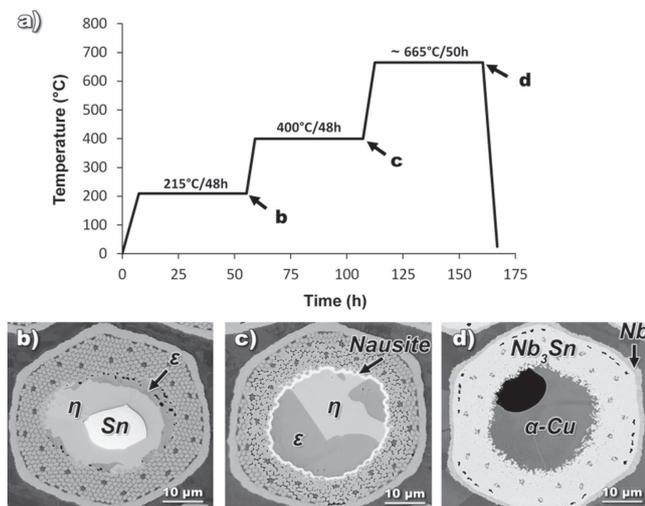

Figure 2. The standard heat treatment (HT) used for RRP® wires since the early 2000s. The heat treatment uses three isothermal steps, each of which has a different effect on the sub-element microstructure, shown here for a 50 μm D_s wire. Backscattered-electron field emission scanning electron microscope (FESEM-BSE) images show the distribution of phases across a sub-element after each HT. Notice a highly irregular penetration of the η phase into the Cu/Nb filament pack after the 215 °C step and, by contrast, the production of a well-defined Nausite ring surrounding the core and much more uniform microstructure between the filament pack and the original Sn core after the 400 °C step.

Figure 3. The Cu–Sn phase diagram. Data extracted from [21].
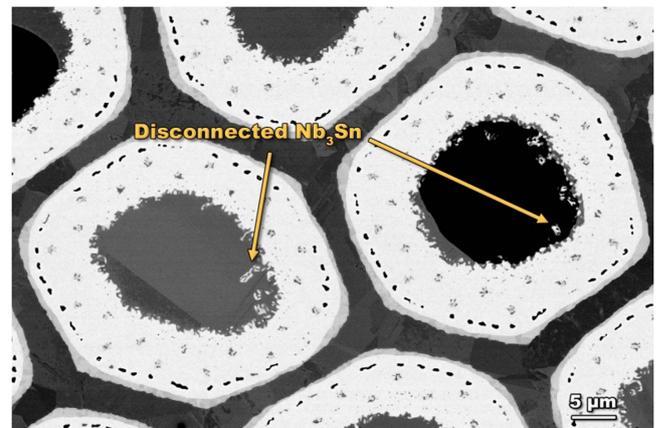
Figure 4. 35 μm sub-elements after a full standard RRP® heat treatment showing a large amount of disconnected Nb$_3$Sn produced by liquefaction of the residual η phase, its reaction to Nausite on heating above 408 °C, and its final decomposition to Nb$_3$Sn above ~600 °C.

215 °C (namely *'wetting the phase boundaries'* [25] to prevent large Kirkendall voids) which will be touched upon in the discussion section of this article.

Although the liquefaction of pure Sn was the main suspect for Sn bursts and their instances are seldom recorded in the literature, the liquefaction of η above 408 °C presents a different challenge that is better recorded. It was noticed for many years that the liquid resulting from the melting of η appeared to be responsible for the dissolution of Nb filaments, creating islands of Nb$_3$Sn upon final reaction [13]. Figure 4 shows a group of sub-elements ($D_s = 35$ μm) where a
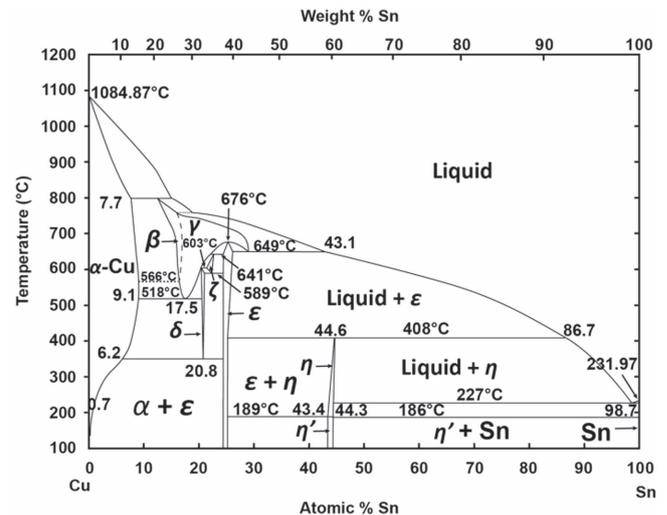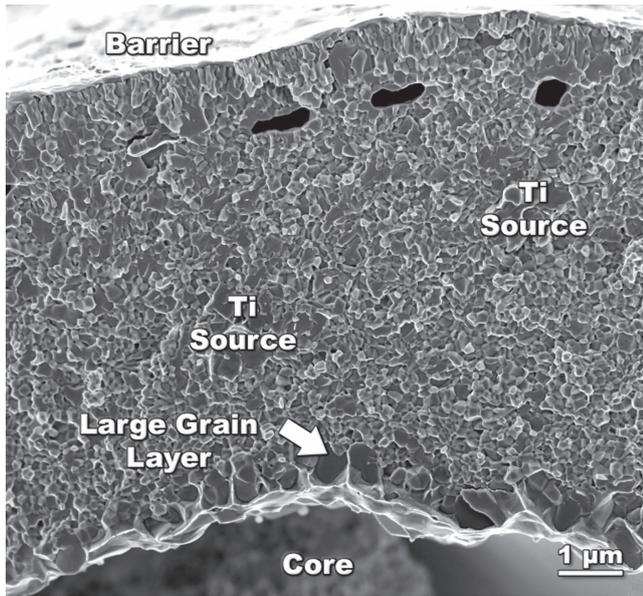
Figure 5. Fractured surface of the A15 layer of a 35 μm sub-elements heat treated using the standard RRP® heat treatment showing a row of coarse-grain A15 where the Nausite ring once was.

significant Nb dissolution occurred, ending up as disconnected pieces of A15 after the full reaction.

Perhaps because the functions of the low-temperature Cu–Sn mixing heat treatments appeared very simple, the 215 °C and 400 °C steps for RRP® have remained relatively unchanged since their introduction [16]. Only the final step (the A15 reaction) has been varied, changing slightly as the RRP® wires improved their doping [14] and their D_s was reduced [8].

1.3. Recent studies of Cu–Sn mixing

In the past 10 years, studies at CERN have questioned the rationale behind some mixing heat treatment steps. For example, Scheuerlein *et al* concluded that the mixing steps '*neither reduce the void volume nor improve the chemical strand homogeneity*' [26] of ITER-type internal-tin wires. They also found that '*long lasting plateaus are counterproductive to J_c*' [27] in high-Sn content internal-tin wires like RRP®, because such wires are susceptible to the formation of Nausite. As it will be shown below, and as suspected in [27, 28], this Nausite phase (the Sn–Nb–Cu ternary phase discovered by Naus *et al* [29] in 2002, and now identified as $Nb_{0.75}Cu_{0.25}Sn_2$ [30]) is the source of Nb dissolution and subsequent coarse-grain A15 formation, which were important suspects for the J_c degradation in RRP® wires. A row of this coarse-grain A15 derived from Nausite can be seen in fractured A15 layer in figure 5 at the inner wall of the A15 ring (bottom of image). In 2013, more detailed studies were performed by Pong *et al* [31] at CERN, showing that a Nausite layer blocks Sn diffusion from the core into the filament pack by creating a continuous ring at the inner walls of the Cu/Nb composite. Pong *et al* found that such a ring was only formed in sub-elements with low Cu content between the Nb filaments (i.e. low local area ratio (LAR) wires), which is indeed the case of the current RRP® sub-element design.
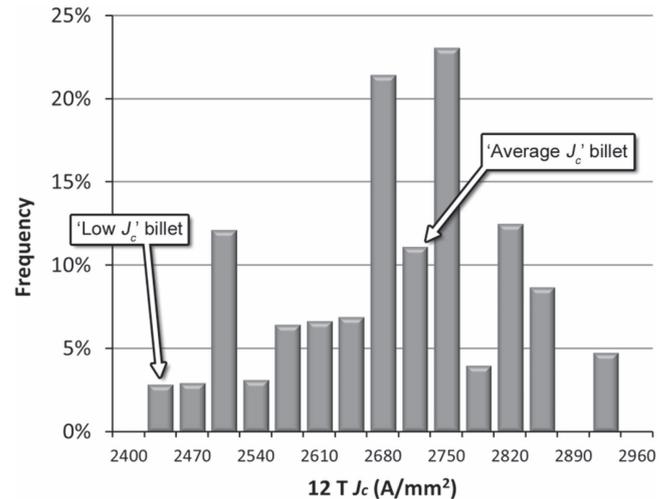

Figure 6. The (12 T, 4.2 K) J_c scatter of a recent production run of 35 billets with the 132/169 configuration 0.85 mm in diameter ($D_s = 50$ μm).

Although much of the focus regarding Nb_3Sn heat treatments has been on diffusion of Sn into the Nb filament pack, Pong *et al* [31] actually pointed out that diffusion of Cu from the Cu–Nb filament pack into the core was the dominant mass migration in the highest J_c wires. This large variety of interpretations of the Cu/Sn mixing process inspired this work to fully explore the phase transformations during these early stages in the heat treatment in order to understand the role of Nausite and its relationship to Nb_3Sn formation in these high-J_c internal-tin wires.

2. Experimental procedures

The wires used in this study are 132/169 stacks (see figure 1(c)) with a Nb:Sn atomic ratio of 3.6:1. Two nominally identical billets allowed exploration of J_c-scatter: one billet has an average 12 T J_c of 2720 A mm^{-2} at a wire diameter of 0.85 mm, when heat treated using the standard heat treatment of figure 2, while the other billet has a 12 T J_c of 2480 A mm^{-2} when heat treated under the same conditions. We show the J_c distribution for a recent 35-billet production run (at 0.85 mm) in figure 6 to provide a better idea of the billet-to-billet scatter. The billets in this study are referred to as 'average J_c billet' and 'low J_c billet'. Additionally, they were drawn to three different sizes: the nominal production size (0.85 mm), as well as 0.7 mm and 0.6 mm with a D_s of 50 μm, 41 μm, and 35 μm respectively (all of which are below the required D_s specification for the current Hi-luminosity upgrade of the LHC [9]). The intention of the smaller diameter wires is not to suggest the use of thinner wires but rather to investigate the effects of the heat treatment in smaller sub-elements, which are also achievable at larger wire diameters in higher stack wires (e.g. 217 stack).

For heat treatment studies, 14 cm long pieces of wire were sealed in in quartz tubes pumped to ~10^{-6} Pa and then back-filled with argon at 300 Torr. A four-zone tube furnace

($\pm 2\,^\circ$C over a length of 20 cm) was used for heat treatment. The tubes were pulled out of the furnace at various times during the heat treatment, and immediately water quenched to rapidly solidify any liquid phases, as well as to prevent solid state phase transformations of the high temperature phases. Small sections of these quenched wires (about 1 cm in length) were then mounted inside a metallographic puck in a transverse orientation, polished, and imaged using the back-scattered-electron detector of a Zeiss 1540 Crossbeam® FESEM, to inspect the phases present. The phases were identified using energy dispersive spectroscopy (EDS) performed at 15 kV using standardless analysis (EDAX TEAM V34) with an EDAX Apollo XP SDD detector. The microstructures were quantified using the open-source image analysis (IA) software Fiji [32] with various macros that have been made available in [33].

After the heat treatment studies, selected critical current I_c measurements were made using separate reaction and testing barrels made of stainless steel and Ti-6Al-4V respectively (as described in [34]). Once the samples were mounted on the testing barrel, four voltage taps (24 cm apart) were soldered and the entire assembly covered with paraffin to fix the sample in place. A criterion of $0.1\,\mu$V cm^{-1} was used to define I_c and n-values were derived from the log V–log I characteristics across the full length of the four voltage taps (72 cm). RRR measurements were performed by measuring resistivity at room temperature (293 K) and 20 K.

3. Results

Because of the complexity of the heat treatment studies, we will separate them into three sections. The first section will summarize the reactions occurring in the standard heat treatment (see figure 2), the second section will focus on the optimization of the (now called) *'Nausite control heat treatment'* (NCHT) which deals with the Nausite ring and its operation as a regulatory membrane, as well as the conversion of the Sn-rich core (made mostly of η) into a lower-Sn core (made mostly of ε). Then, in the final section, we explore the significant critical current density improvements that result from the NCHT.

### 3.1. Standard two-stage Cu/Sn mixing heat treatment results

As the Sn diffuses outwards into the surrounding Cu during the initial mixing at 215 °C, it does so with the expected neighboring phases, forming η on the Sn side and ε on the Cu side. Small Kirkendall voids are commonly seen at random places between the Cu and the ε phase, and large Kirkendall voids are occasionally seen at the core center. As the 215 °C mixing stage proceeds, the Sn diffusion seems to significantly slow once the Cu–Sn phases reach the filament pack, causing the η phase to consume the ε in some regions. Very rarely does the ε phase penetrate into the filament pack; however, in certain instances, the η phase does seem to penetrate a few filament rows along with a higher Sn phase (most likely Nausite)
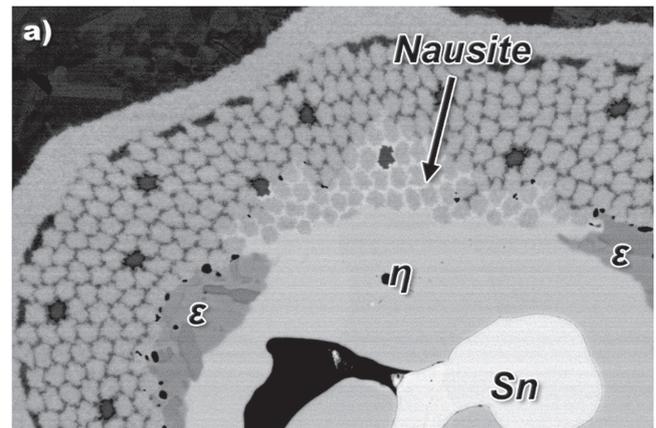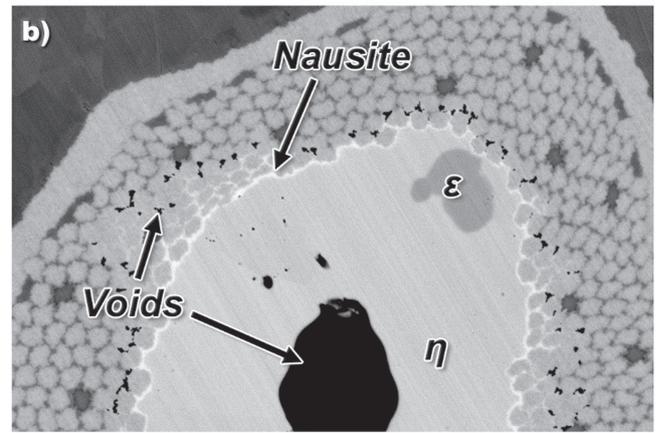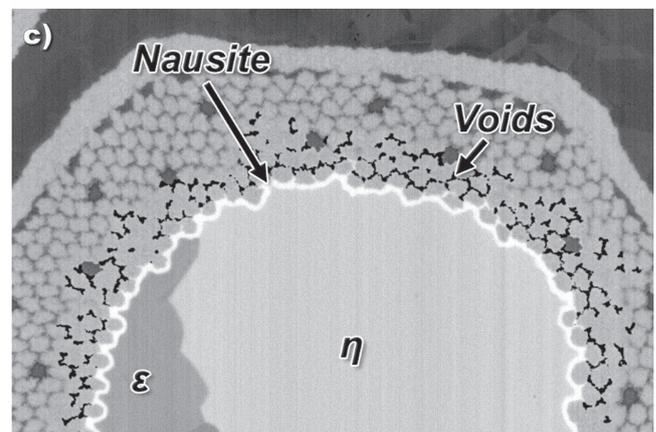
Figure 7. FESEM-BSE details from sub-elements at different stages of the standard heat treatment. (a) At the end of the 215 °C step, some irregular Nausite has formed within the filaments, sometimes into the fourth row of filaments. (b) At the beginning of the 400 °C heat treatment step, voids within the filaments are indicative of Cu diffusing into the core through a thin Nausite layer (the white ring). (c) Eight hours into the 400 °C step where Nausite has now receded into a uniform, thin Nausite ($Nb_{0.75}Cu_{0.25}Sn_2$) ring, leaving many voids in what was originally the Cu matrix around the Nb filaments.

around some of the filaments. All of the above mentioned aspects of the 215 °C step can be observed in figure 7(a). It is very important to point out that the 48 h at 215 °C do not consume all of the Sn present in the wires—something that was pointed out in [24, 35] for similar wire types—about 30% of the initial Sn remains and liquefies once the heat treatment proceeds to the 400 °C mixing stage.

At the beginning of the 400 °C step (figure 7(b)) we observe the beginning of the Nausite ring and the conversion of the interfilamentary η penetration to a high-Sn phase consistent in picture-contrast with the Nausite ring. Images of the wires at the 400 °C step confirm that a continuous Nausite ring forms at the inner perimeter Cu/Nb filament pack during this step (as described by Pong *et al* [31]). This uniform Nausite ring is formed even in the above mentioned instances where η or Nausite had penetrated the filament pack at 215 °C. The ring does not penetrate beyond the first or second row of filaments in contrast to the ring shown by Naus [29] for a high-J_c MJR wire (24 h/362 °C). Furthermore, during the 400 °C step, we observed that a large fraction of the interfilamentary Cu migrates from the filament pack into the core through the Nausite ring, something that was not evidenced for the different wires in [31] at this point in the reaction. Such Cu migration was assumed by the increased amount of the Cu-rich ε phase (Cu 25 at%Sn) in the sub-element cores and by the presence of voids within the filaments (as seen in figure 7(c)). Comparing the images in figure 7, it is evident that the radial distribution of phases becomes much more homogeneous during the 400 °C heat treatment. Figure 8 uses a single sub-element example to demonstrate the evolution of the Nausite ring thickness during the 400 °C mixing stage and the relative amounts of ε, η, and voids. Similar measurements will be shown in the next section for larger data sets.

The important features of the mixing stages of the standard heat treatment shown in figures 7 and 8 are:

1. During the ramp to the 215 °C step, only minimal diffusion of Sn into the Cu-annulus occurs (the Cu-annulus being the Cu region separating the Sn core and the Cu/Nb filament pack).
2. During the 215 °C isothermal step, Sn penetrates irregularly one to two filaments deep (and in typically one isolated region per sub-element three to four filaments deep) into the Cu/Nb filament pack; transforming the Cu matrix around a few Nb filaments into a high-Sn phase which (although difficult measure using EDS) is most likely Nausite given its similar atomic number contrast to the thicker Nausite ring (figure 7(a)).
3. At the end of the 215 °C step, the sub-element core (i.e. Sn core + Cu-annulus) transforms into a mixture of about 60% η and ε, and 40% residual Sn.
4. During the ramp to 400 °C, a thin Nausite layer forms around the inner filaments while at the same time receding from earlier and deeper penetration of the filament pack, even the deep penetration regions.
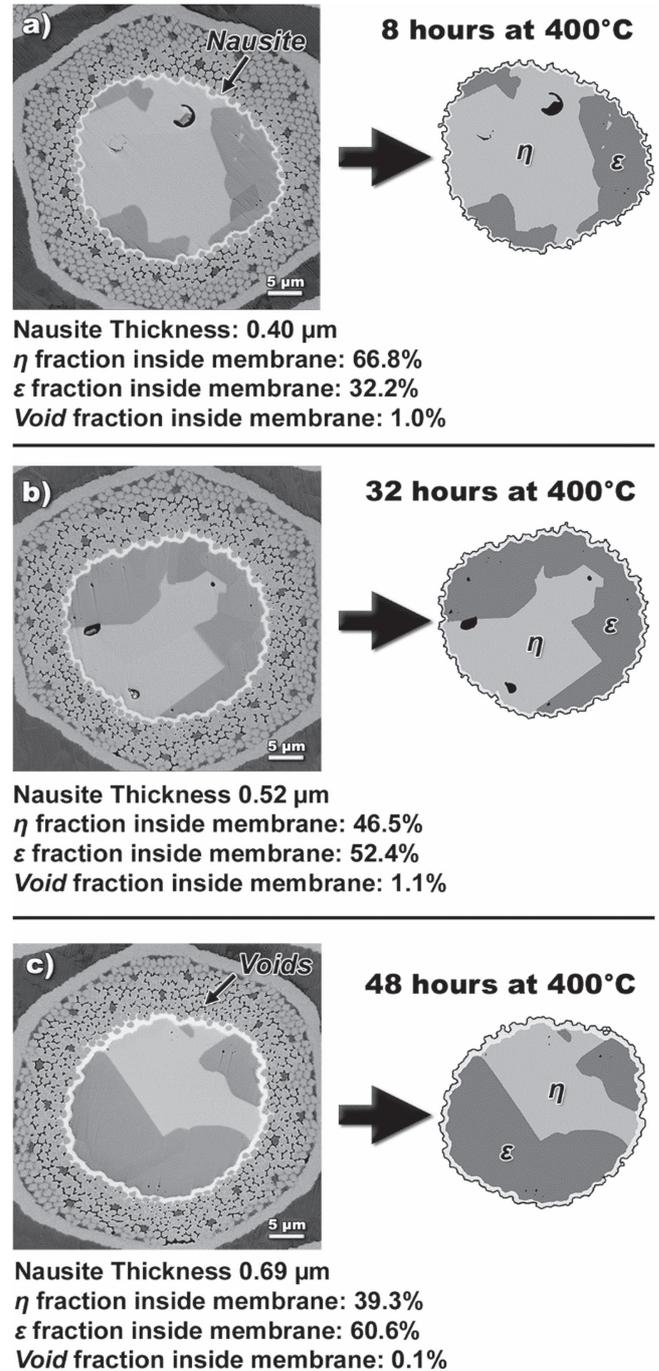

Nausite Thickness: 0.40 μm
η fraction inside membrane: 66.8%
ε fraction inside membrane: 32.2%
Void fraction inside membrane: 1.0%

Nausite Thickness 0.52 μm
η fraction inside membrane: 46.5%
ε fraction inside membrane: 52.4%
Void fraction inside membrane: 1.1%

Nausite Thickness 0.69 μm
η fraction inside membrane: 39.3%
ε fraction inside membrane: 60.6%
Void fraction inside membrane: 0.1%

Figure 8. A sub-element heat treated with a first stage of 48 h at 215 °C and after (a) 8 h, (b) 32 h, and (c) 48 h at 400 °C. The measured sub-micron Nausite thickness and the η, ε, and void fractions are also indicated.

Interfilamentary Kirkendall voids now appear where the Cu (or the Nausite) originally was (figure 7(b)).

5. During the 400 °C step, the Nausite layer becomes much better defined, forming a remarkably uniform ~0.5 μm thick ring separating the sub-element core from the filament pack. Voids appear around filaments where Cu used to be and the Sn core transforms into a mixture of η and ε phases confined inside the Nausite
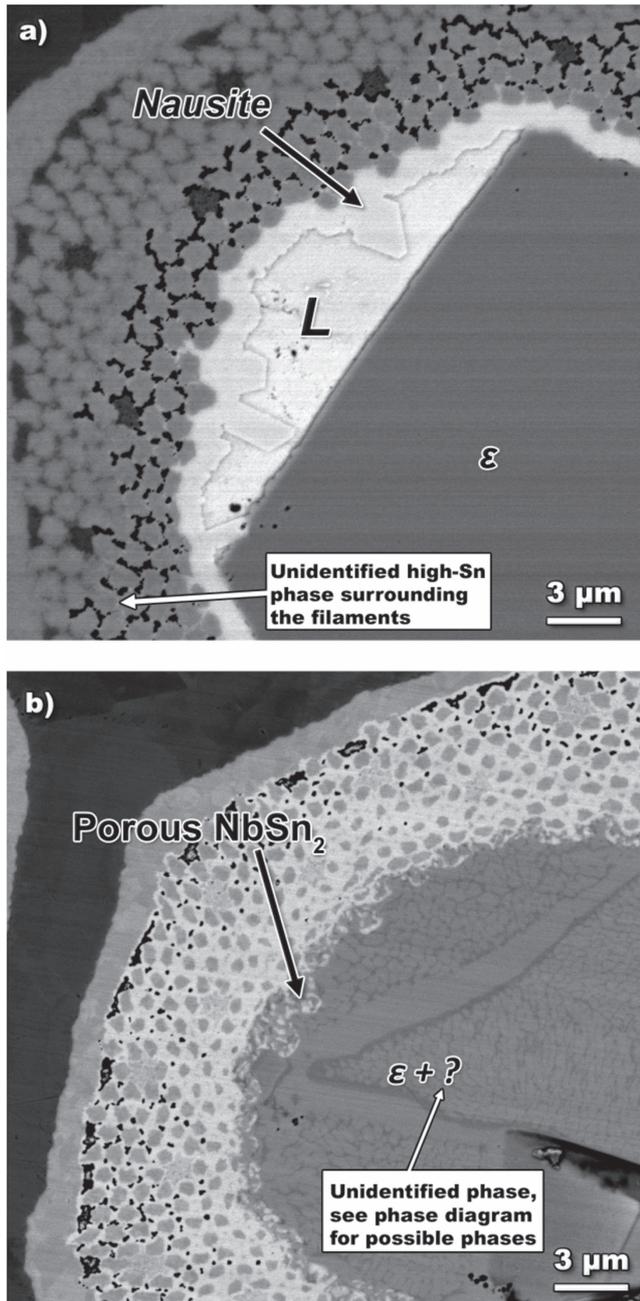
Figure 9. Quenched microstructures of a sub-element during the standard heat treatment ramp at (a) 500 °C and (b) at the end of the ramp when the temperature first reached the final A15 reaction step at 665 °C. L = location of liquid phase prior to quench.

Table 1. Nausite control heat treatments (NCHT) used to explore Cu diffusion and Nausite layering thickness evolution.

ID	Sn mix step	Nausite control step	A15 reaction
A	No	250 °C for 150 h	665 °C for 50 h
B	No	300 °C for 150 h	665 °C for 50 h
C1	No	350 °C for 150 h	665 °C for 50 h
C2	No	350 °C for 400 h	620 °C for 600 h
C3	No	350 °C for 400 h	665 °C for 50 h
D	No	360 °C for 150 h	665 °C for 50 h
E	No	370 °C for 104 h	665 °C for 50 h
F	No	380 °C for 104 h	665 °C for 50 h
G	No	390 °C for 104 h	665 °C for 50 h
H	No	398 °C for 48 h	665 °C for 50 h
Std.	215 °C for 48 h at	398 °C for 48 h	665 °C for 50 h

(figure 9(b)). On further heating, the $NbSn_2$ transforms via Nb_6Sn_5 into the disconnected pieces of Nb_3Sn (associated with the so-called Nb dissolution of figure 4), as well as coarse A15 grains characteristic of low performance wires [27]. Finally, during the 665 °C step (A15 reaction), Nb_3Sn forms rapidly throughout the filament pack (as observed by the large extent of reaction in figure 9(b)).

3.2. Rethinking the Cu–Sn mixing heat treatment by optimizing growth of a thin Nausite membrane layer

The quench experiments described above suggest that the most important part of the Cu/Sn mixing reaction occurs at the 400 °C step, while the 215 °C step in fact produces a highly irregular reaction into the Cu matrix (figure 7(a)). Accordingly, 14 production billets were reacted *with and without* the 215 °C step. This included wires with sub-element sizes ranging between 55 and 35 μm, with some 108/127 stacks and some 132/169 stacks (as well as our 'average J_c' and 'lower J_c' billets). The average 16 T I_c difference between the standard 215 °C/400 °C and a single 400 °C step of all the 14 billets was only −0.2% (see next section for a more detailed J_c comparison). Examining the microstructures formed during the reaction, it was observed that a well-developed Nausite ring is reached with or without the 215 °C step.

Guided by the above observations, we set out to re-optimize the Cu–Sn mixing heat treatment with the specific goals of minimizing the amount of Nausite formation, making it into as thin and uniform a layer as possible while at the same time maximizing the desirable diffusion of Cu into the Sn core so as to leave as small a residue of η phase as possible at the end of the mixing step. We concentrated on lowering the temperature of the 400 °C step to reduce the Nausite ring thickness, and used longer diffusion times to enable more Cu to diffuse into the core so as to maximize the ε fraction in the core. The various heat treatments used are shown in table 1. Note that we lowered the standard 400 °C plateau to 398 °C since it was recently found that the melting point of η is 408 °C, 7 °C lower than previously thought [21]. 398 °C provides a 10 °C margin, which we believe is sufficient for

ring (figure 8(c)). Randomly situated voids in the core are now sometimes observed.

After both mixing stages are complete, a critical event unfolds: during the ramp to 665 °C, the residual η phase liquefies above 408 °C, and large faceted grains of Nausite grow into the liquid wherever it is in contact with the Nausite ring, as shown in figure 9(a). Nausite has been suspected to decompose into $NbSn_2$ [27], and our observations confirm this, given that these Nausite grains (as well as the Nausite ring itself) decompose into porous structures of $NbSn_2$
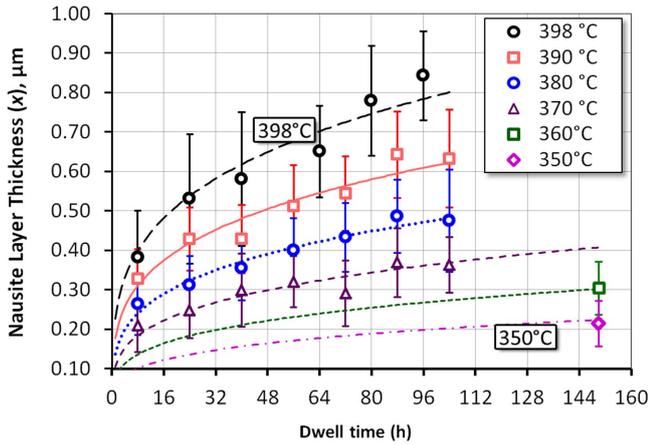
Figure 10. Nausite layer thickness measured using IA algorithms with least-square fits for data points above 370 °C. Predicted layer thicknesses for 350 °C and 360 °C agree well with the observations.

Figure 11. Sn composition of the sub-element cores as a function of time for the 'average J_c billet' at 0.85 mm in diameter. These values are calculated from the measured area fractions of the η and ε phases in the core assuming they are line compounds of 44.6 at%Sn and 25.0 at%Sn respectively.

most applications. Additionally, it is also worth noting that the 215 °C stage was skipped in most of these heat treatments (see next section for its effects on J_c), and that Sn bursts were never observed in these round wires (see discussion for comments on skipping the 215 °C step in cables).

In order to assess the effectiveness of the different NCHTs proposed, IA algorithms were used on the micrographs of quenched wires to measure the η and ε fractions in the core, as well as the Nausite thickness in the manner shown earlier in figure 8.

The Nausite ring growth of the 'average J_c billet' and 'lower J_c billet' was measured, and we determined that the ring thickness increases at the same rate regardless of billet type or sub-element size. Moreover, the Nausite ring has the same thickness and growth rate with or without the 215 °C step. Figure 10 shows the Nausite thickness at various temperatures (for the 'average J_c billet' at 0.85 mm diameter) where each thickness data point is an average of more than eleven thousand measurements done by IA on high magnification images that cover three sub-elements with their respective Nausite rings. The error bars in this graph are the standard deviations of these measurements. Least-square fits were added to the data points of the heat treatments at or above 370 °C, giving a power law growth exponent of 0.27. Using the power law, combined with the Arrhenius equation (1), the activation energy, Q_g, of Nausite membrane growth was found to be 98.3 kJ mol^{-1}, where R is the ideal gas constant and k^0 is a constant. With this, the layer thickness values for temperatures below 370 °C were predicted. The single data points in figure 10 for 360 °C and 350 °C are consistent with the predictions.

$$x(T, t) = \left(k^0\, e^{\left(-\frac{Q_g}{RT}\right)}\right)t^{0.27}. \tag{1}$$

The at%Sn inside the Nausite ring was measured by IA of low magnification images of over 30 sub-elements, assuming that the η and ε phases are line compounds with 44.6 at%Sn and 25.0 at%Sn respectively (see figure 3), and using the specific volumes in [36]. Figure 11 shows that the
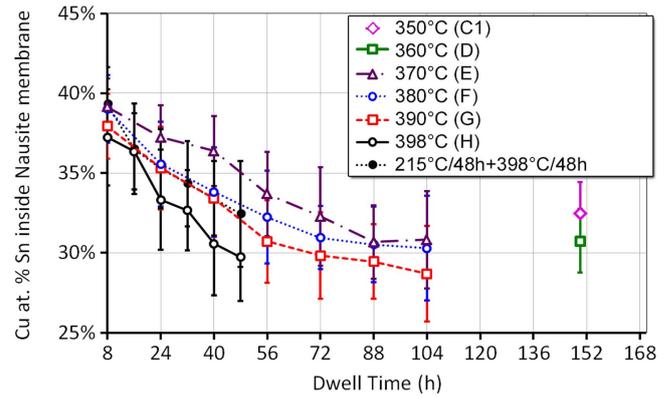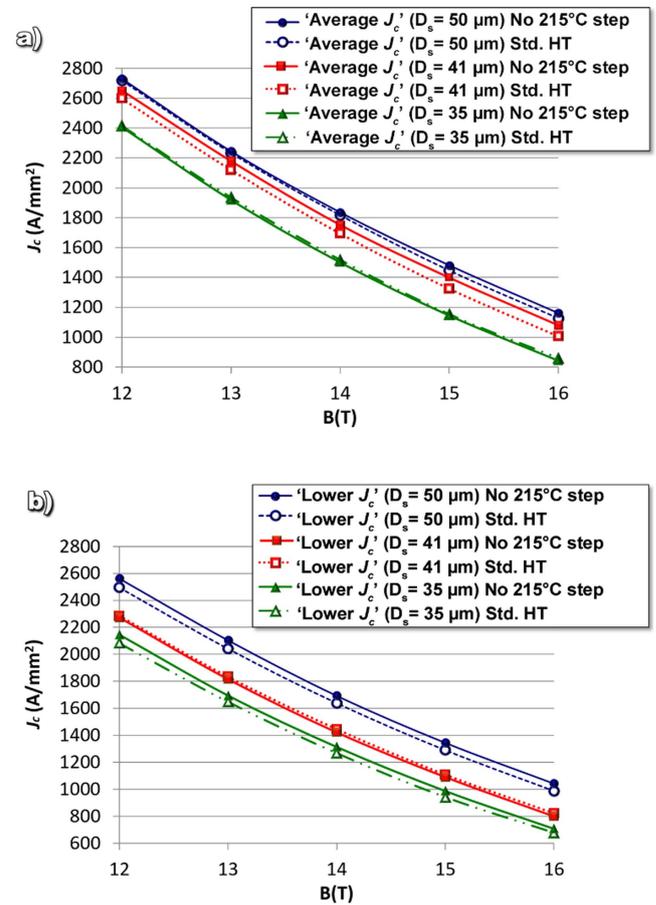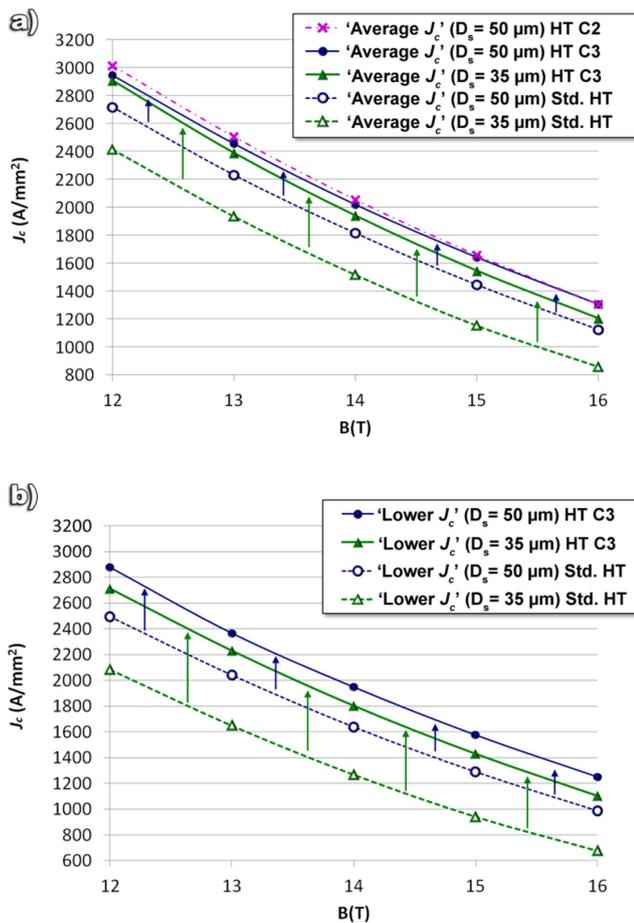

Figure 12. Comparison of the J_c measurements at 0.85 and 0.6 mm diameter using a single mixing heat treatment at 400 °C (solid symbols and curves) compared to the standard two-step Cu/Sn mixing heat treatment (open symbols and dashed curves). The results show that dropping the 215 °C has little or no impact on final J_c.

at.%Sn inside the Nausite rings of the 'average J_c billet' at 0.85 mm in diameter for the heat treatments between 350 °C and 398 °C, falls almost to 30 at%Sn. Two things are worth mentioning here that may alter the true values of figure 11 slightly. One, is the fact that some Sn in the core is

Table 2. Electromagnetic properties obtained using the standard, two-step Cu–Sn mixing heat treatment, and one omitting the 215 °C step.

ID	D_s (μm)	Standard (Std.) HT			Skipping 215 °C step (HT A)			Changes		
		J_c (12 T) (A mm^{-2})	J_c (16 T) (A mm^{-2})	H_k (T)	J_c (12 T) (A mm^{-2})	J_c (16 T) (A mm^{-2})	H_K (T)	ΔJ_c % (12 T)	ΔJ_c % (16 T)	ΔH_K (T)
'Lower J_c'	50	2494	988	24.37	2560	1042	24.72	3%	5%	0.3
'Lower J_c'	41	2284	822	23.28	2273	800	23.07	0%	−3%	−0.2
'Lower J_c'	35	2083	676	22.31	2145	707	22.49	3%	5%	0.2
'Average J_c'	50	2719	1126	25.00	2730	1161	25.43	0%	3%	0.4
'Average J_c'	41	2598	1006	24.09	2650	1080	24.77	2%	7%	0.7
'Average J_c'	35	2415	859	23.12	2407	844	23.01	0%	−2%	−0.1
Average	—	2432	913	23.70	2461	939	23.91	0.9%	2.7%	0.22

Figure 13. Comparison of the J_c measurements at 0.85 and 0.6 mm diameter using the new, single step (400 h at 350 °C) Nausite control heat treatment, compared to the standard two-step Cu/Sn mixing heat treatment.

being transformed into Nausite, causing the at%Sn to drop at a faster rate for high temperatures because of the faster Nausite layer growth rate. And two, η is not truly a line compound and at lower temperatures it can have a wider composition range [37].

Since it is clear from figure 11 that longer times allow more Cu diffusion, and it is also clear from figure 10 that a lower temperature significantly reduces the Nausite membrane thickness, we decided to replace the two-step mixing

process with a single NCHT at 350 °C for 400 h, followed by the usual 665 °C 50 h A15 reaction. Such a heat treatment is labeled HT C3 in table 1, and its effects are discussed in the section below.

3.3. Reactions with single step Cu–Sn mixing reactions

The effects of skipping the 215 °C step on critical current density, J_c, in the standard two-step mixing HT are negligible as is clearly shown by the measurements in figure 12, as well as the values shown in table 2 (including the effects on the Kramer field, H_K).

The effects of replacing the standard two-step Cu/Sn mixing heat treatment by a single step at 350 °C for 400 h (Nausite control HT C3) are more dramatic and important than those skipping the 215 °C step. Figure 13 shows a significant increase of J_c for HT C3. For example, the widely reported J_c (12 T) metric improves in the best case from 2720 to 2950 A mm^{-2} and the best J_c (16 T) values improve even more from 1130 to 1300 A mm^{-2}. HT C2 is also added to this graph ('average J_c' billet only) to show a lower temperature 620 °C alternative to the A15 reaction. The most relevant information is also tabulated in table 3, which shows substantial increases in J_c (an average of 36% at 16 T) and H_K (an average of 1.68 T) for all wires using HT C3 over the standard HT. The lowest 12 T J_c increase in table 3 (8%), corresponds to 764 A of I_c when using HT C3 and 705 A when using the standard HT.

It is also important to point out that the J_c increases was not bought at any price to the RRR of these wires, which averaged 200, the same as that obtained when using the standard HT. Figure 14 shows the J_c values as a function of H_K and here too we see a significant improvement using HT C3. These wires now achieve higher J_c and higher H_K with a reduced spread. The relative improvements in H_K and J_c with HT C3 are even more marked as the sub-element size is reduced (figure 15).

4. Discussion

Our studies have shown that the standard two-step Cu/Sn mixing heat treatment empirically developed more than a decade ago and stable for many years of internal-tin wire

Table 3. Electromagnetic properties obtained using the standard heat treatment and a Nausite control heat treatment at 350 °C for 400 h.

|		Standard (Std.) HT			Single 350 °C Nausite control step (HT C3)			Changes		
ID	D_s (μm)	J_c (12 T) (A mm^{-2})	J_c (16 T) (A mm^{-2})	H_k (T)	J_c (12 T) (A mm^{-2})	J_c (16 T) (A mm^{-2})	H_k (T)	ΔJ_c % (12 T)	ΔJ_c % (16 T)	ΔH_k (T)
'Lower J_c'	50	2494	987.65	24.37	2878	1251	25.77	15%	27%	1.40
'Lower J_c'	41	2284	822.37	23.28	2798	1171	25.13	23%	42%	1.85
'Lower J_c'	35	2083	676.26	22.31	2713	1104	24.74	30%	63%	2.43
'Average J_c'	50	2719	1126	25.00	2946	1307	26.10	8%	16%	1.10
'Average J_c'	41	2598	1006.4	24.09	2979	1296	25.76	15%	29%	1.67
'Average J_c'	35	2415	859.04	23.12	2910	1207	25.01	20%	41%	1.89
Average	—	2432	913	23.70	2871	1223	25.42	19%	36%	1.72
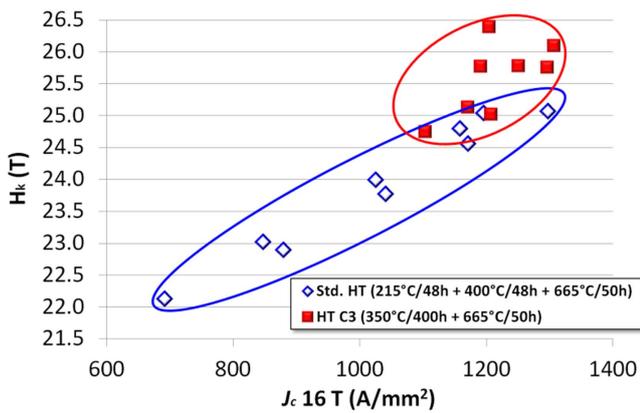
Figure 14. J_c (16 T) measurements as a function of Kramer field (H_k) of the billets in discussion (all billets in table 3) using the standard HT and HT C3.

Figure 15. Increase in H_K and J_c from standard HT to HT C3 as a function of sub-element size.

evolution is in fact not optimized for RRP® (and presumably other similar high-J_c wires that develop a Nausite ring). Our detailed studies of the Cu/Sn mixing step have shown that full Cu–Sn mixing does not take place inside the filament pack for these low LAR internal-Sn composites. A key insight of the present work is that it is highly valuable to form a well-controlled Nausite ring between the filament pack and the Sn core because the ring appears to act like a membrane that
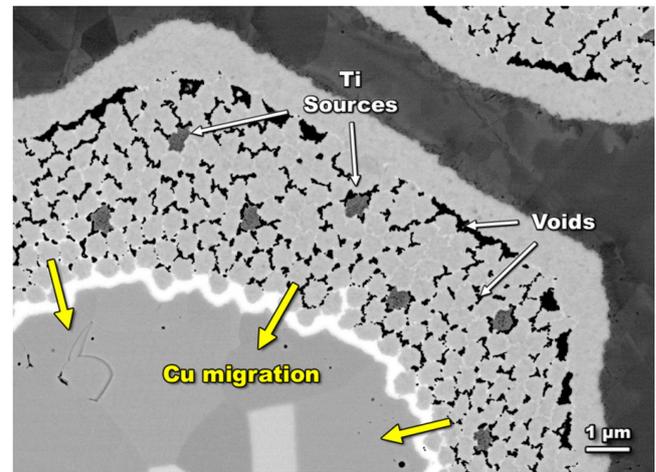

Figure 16. FESEM-BSE image of a sub-element at the end of the Nausite control HT at 350 °C that shows the almost complete migration of the Cu from the filament pack into the core (even from the filament/barrier interface).
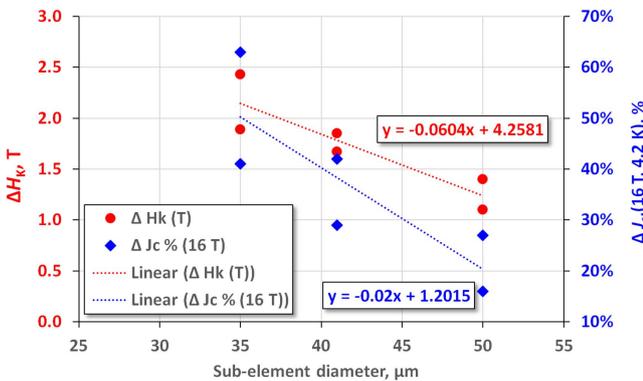
osmotically allows inward Cu diffusion from the filament pack into the core while limiting outward Sn diffusion into the filament pack. The important impact of this diffusion of Cu into the Sn is to convert the low melting Sn and η phases into a largely ε phase which remains solid during the highest temperature A15 reaction step. We show here that the controlled growth of the regulating thin Nausite layer is best performed by replacing the present mixing steps at 215 °C and 400 °C by a single Nausite control step at about 350 °C. The benefits of this simplified heat treatment appear to be multiple: (1) A more complete diffusion of Cu into the sub-element core from the filament pack, minimizing the amount of η phase left after the single step reaction at ~350 °C, (2) minimizing liquefaction above 408 °C and the formation of coarse-grain or disconnected Nb₃Sn, and (3) minimizing the withdrawal of Nb from the filament pack to make the $(Nb_{0.25}Cu_{0.75})Sn_2$. The net effect is a significantly more effective Nb₃Sn layer with higher J_c and higher irreversibility field particularly at smaller sub-element diameters. The use or omission of the 215 °C step seems to have no effects on round wires, however its effects on Sn bursting are currently being studied in cables.

Table 4. The void area % inside the sub-element core at the end of the Nausite control step averaged over all billets in discussion.

Heat Treatment	Sn mix step	Nausite control step	Void area %
D		360 °C for 150 h	0.42%
E		370 °C for 104 h	0.48%
F		380 °C for 104 h	0.67%
G		390 °C for 104 h	1.40%
H		398 °C for 48 h	1.90%
Std. (398 °C)	215 °C for 48 h	398 °C for 48 h	1.10%

4.1. On interfilamentary voids

Our studies also show that RRP® wires can form high quality Nb$_3$Sn even when a substantial number of voids surround the Nb filaments prior to the final Nb$_3$Sn formation. With the optimization of the NCHT described in this work, the Cu in the filament pack can be almost completely diffused into the core, leaving a majority of interfilamentary void space behind as shown in figure 16. Extensive concerns about Kirkendall voids have historically been expressed because of the belief that voids limit diffusion, harm A15 homogeneity, and may initiate cracks [38–41]. The fact that the new heat treatment process described here increases the interfilamentary void space (compare figure 9(a) with figure 16) while also ultimately improving the quality of the A15 shows that the development of a homogeneous Cu–Sn matrix around the filaments is not necessary. Instead, it appears that once the Nausite barrier decomposes, the Sn can readily diffuse into the filament pack through a thin layer of a Sn-rich phase at the filament surface (inferred by the high atomic contrast seen right before the Nb$_3$Sn reaction, see figures 9(a) and 16). The ability of Sn to react on the periphery of filaments seemingly surrounded by voids is consistent with the lack of reported relationships between interfilamentary voids and significant compositional inhomogeneities in the final A15 layer despite the many studies on a wide variety of Nb$_3$Sn wires [19, 42–44].

4.2. On Sn core voids and the 215 °C step

Large Kirkendall voids at the center of the sub-elements have also been suspected to be detrimental to wire performance [17]. This suspicion has been often a justification for the 215 °C step, since such a step appears to '*wet the Cu/Sn phase boundaries*' [19], and therefore suppresses the formation of large voids (one of which is seen even at the second stage of the standard HT in figure 7(b)). However, for our samples, we can control the void formation by playing with the temperature of the second mixing step. Table 4 has the measured void fractions inside the sub-element cores at the end of various NCHT temperatures (averaged over all billets in table 2). This table shows that the void fraction decreases with the NCHT temperature and is significantly lower for the NCHTs at 380 °C and below, which is yet another benefit of lowering the temperature (assuming that large voids are indeed detrimental to wire properties). It must be said that skipping the 215 °C step *does* produce more voids when the

same temperature is used (compare HT H to Std. HT), however the temperature is much more influential than the presence or absence of the 215 °C step (compare HT G to HT E).

4.3. The NCHT

There are two components of the NCHT that appear to be responsible for the success of HT C3. The first is the reduced thickness of the Nausite layer (55% thinner than that of the standard HT) resulting from the low temperature. The second characteristic is the increased volume of interfilamentary Cu that diffuses into the core due to the longer time, resulting in a lower amount of η before its liquefaction. These two attributes of the NCHT minimize the amount of Nb lost to dissolution and therefore increase J_c. However, although the increase in J_c can easily be attributed to better A15 connectivity, the increase in H_K may be related to an enhanced quality of the A15. Given that the A15 step was not altered in this study (with the exception of HT C2), it is possible that the lower H_K values in the standard. HT are related to the coarse-grain (but still connected) A15 derived from the Nausite membrane. Another area of unknown impact may be on the distribution of the Ti dopant (which is key to obtaining high H_K values in these composites) that relies on uniform diffusion from the Nb-47Ti rods and temperatures above those covered by this study. It could be that the more uniform and controlled filament pack achieved by the NCHT is beneficial to promoting a homogeneous distribution of Ti.

The thickness of the Nausite layer is expected to be independent of sub-element diameter, thus the Nb lost to its formation will become a greater component of the sub-element as the sub-element diameter is reduced. For this reason Nausite control becomes more and more important as high-J_c wires are driven to smaller D_{eff}. As shown in figure 15, the relative increase in J_c and H_K with the adoption of the new NCHT increases significantly as the sub-element diameter is decreased.

Finally, given that the benefits of such a long heat treatment (HT C3) are less dramatic for larger sub-elements, an important alternative is HT E. This NCHT is similar in length to the standard HT and it has strong positive effects for low-performing billets even at 50 μm D_s (similar to the larger effects seen for the 'lower J_c' billet at 50 μm, see the blue/dark arrows of figure 13). It is expected that HT E will narrow the billet J_c-scatter towards the upper values (similar to that of

figure [14]) and therefore be of great value to current wire designs for the Hi-luminosity LHC upgrade.

5. Conclusion

By quantifying the microstructural changes that occur during heat treatment of high-J_c internal-tin wires, we have identified the key role of the 'Nausite membrane' in controlling Cu and Sn inter-diffusion. Using this knowledge we developed a new heat treatment schedule for RRP® wires that significantly improves the on so-called Cu–Sn 'mixing' steps, producing an average increase in 16 T J_c of 36% across several billets at various sizes—with very good RRR values. We have shown that controlling the Nausite layer is crucial for the inhibition of Nb dissolution (which results in disconnected islands of Nb$_3$Sn that do not contribute to current transport) as well as coarse-grain Nb$_3$Sn (which reduces the local pinning site density in the A15 layer). By controlling the formation and the thickness of the Nausite layer, we can increase the Cu:Sn ratio in the sub-element cores and thus decrease the η phase fraction before crossing the melting temperature of the η phase. This is achieved using a heat treatment with a single *Nausite control* stage at 350 °C for 400 h (where a mixing heat treatment at 215 °C is optional and has no effects on J_c). We also show that this heat treatment results in an increasingly dramatic improvement in J_c as the sub-element size decreases, allowing a 16 T J_c of 1200 A mm^{-2} with a D_{eff} (or D_s of 35 μm), and bringing us closer than before to the FCC targets of 1500 A mm^{-2} at 16 T with a D_{eff} of 20 μm. An alternative (shorter) heat treatment with a single *Nausite control* stage at 370 °C for 104 h can still provide a positive impact on the J_c of low-performing billets at $D_s > 50$ μm, allowing billet J_c-scatter to narrow significantly.

Acknowledgments

ORCID iDs

Charlie Sanabria ● https://orcid.org/0000-0001-5017-5309
Peter J Lee ● https://orcid.org/0000-0002-8849-8995

References

[1] Nakada T *et al* 2013 *The European Strategy for Particle Physics Update 2013* CERN (European Strategy Session of Council 16th Session)

[2] Benedikt M and Zimmermann F 2016 Towards future circular colliders *J. Korean Phys. Soc.* **69** 893–902

[3] Benedikt M and Zimmermann F 2016 *Status and Challenges of the Future Circular Collider Study* CERN-ACC-2016-0005 (Geneva: CERN) https://cds.cern.ch/record/2120816

[4] Brüning O S, Collier P, Lebrun P, Myers S, Ostojic R, Poole J and Proudlock P (ed) 2004 *LHC Design Report* CERN-2004-003-V-1 (Geneva: CERN) (https://doi.org/10.5170/CERN-2004-003-V-1)

[5] Schoerling D *et al* 2015 Strategy for superconducting magnet development for a future hadron-hadron circular collider at CERN *Proc. Science, The European Physical Society Conf. on High Energy Physics*

[6] Rossi L 2010 Superconductivity: its role, its success and its setbacks in the Large Hadron Collider of CERN *Supercond. Sci. Technol.* **23** 034001

[7] Ballarino A and Bottura L 2015 Targets for R&D on Nb$_3$Sn conductor for high energy physics *IEEE Trans. Appl. Supercond.* **25** 6000906

[8] Field M B, Zhang Y, Miao H, Gerace M and Parrell J A 2014 Optimizing conductors for high field applications *IEEE Trans. Appl. Supercond.* **24** 6001105

[9] Cooley L D, Ghosh A K, Dietderich D R and Pong I 2017 Conductor specification and validation for high-luminosity LHC quadrupole magnets *IEEE Trans. Appl. Supercond.* **27** 6000505

[10] Parrell J A *et al* 2009 Internal tin conductors engineered for fusion and particle accelerator applications *IEEE Trans. Appl. Supercond.* **19** 2573–9

[11] Parrell J A, Zhang Y, Field M B and Hong S 2007 Development of internal tin Nb$_3$Sn conductor for fusion and particle accelerator applications *IEEE Trans. Appl. Supercond.* **17** 2560–3

[12] Field M B, Parrell J A, Zhang Y, Meinesz M and Hong S 2008 Internal Tin Nb$_3$Sn conductors for particle accelerator and fusion applications *Adv. Cryog. Eng. Mater.* **986** 237–43

[13] Parrell J A, Zhang Y, Field M B, Cisek P and Hong S 2003 High field Nb$_3$Sn conductor development at Oxford Superconducting Technology *IEEE Trans. Appl. Supercond.* **13** 3470–3

[14] Ghosh A K, Cooley L D, Parrell J A, Field M B, Zhang Y and Hong S 2007 Effects of reaction temperature and alloying on performance of restack-rod-process Nb$_3$Sn *IEEE Trans. Appl. Supercond.* **17** 2623–6

[15] Tarantini C, Lee P J, Craig N, Ghosh A and Larbalestier D C 2014 Examination of the trade-off between intrinsic and extrinsic properties in the optimization of a modern internal tin Nb$_3$Sn conductor *Supercond. Sci. Technol.* **27** 065013

[16] Field M, Parrell J, Zhang Y and Hong S 2006 Critical current density in Nb$_3$Sn superconducting wire *US Patent* US20060081307 A1

[17] Smathers D B 1990 Process for making filamentary superconductors using tin-magnesium eutectics *US Patent* US4973527 A

[18] Zhang Y, McKinnell J C, Hentges R W and Hong S 1999 Recent development of niobium-tin superconducting wire at OST *IEEE Trans. Appl. Supercond.* **9** 1444–6

[19] Schwall R, Ozeryansky G, Hazelton D, Cogan S and Rose R 1983 Properties and performance of high current density Sn-core process MF Nb$_3$Sn *IEEE Trans. Magn.* **19** 1135–8

[20] Sanabria C 2017 A new understanding of the heat treatment of Nb$_3$Sn superconducting wires *PhD Thesis* Florida State University

[21] Fürtauer S, Li D, Cupid D and Flandorfer H 2013 The Cu–Sn phase diagram: I. New experimental results *Intermetallics* **34** 142–7

[22] Naus M T, Lee P J and Larbalestier D C 2001 The influence of the starting Cu–Sn phase on the superconducting properties of subsequently reacted internal-Sn Nb$_3$Sn conductors *IEEE Trans. Appl. Supercond.* **11** 3569–72

[23] Rey J M, Barzi E, Mattafirri S, Hoffman J and Yamada R 2002 Effect of partially reacting Nb$_3$Sn before magnet winding on the strand critical current *AIP Conf. Proc.* **614** 1001–7

[24] Mattafirri S, Barzi E, Fineschi F and Rey J M 2003 Kinetics of phase growth in the Cu–Sn system and application to composite Nb$_3$Sn strands *IEEE Trans. Appl. Supercond.* **13** 3418–21

[25] Smathers D 2016 private communication

[26] Scheuerlein C, Michiel M D and Haibel A 2007 On the formation of voids in internal tin Nb$_3$Sn superconductors *Appl. Phys. Lett.* **90** 132510

[27] Scheuerlein C *et al* 2011 Coarse grain formation and phase evolution during the reaction of a high Sn content internal tin strand *IEEE Trans. Appl. Supercond.* **21** 2554–8

[28] Pong I, Oberli L-R, Bottura L and Scheuerlein C 2011 Longitudinal and transverse cross-sectional microstructure and critical current density in superconductors *IEEE Trans. Appl. Supercond.* **21** 2537–40

[29] Naus M 2002 *Optimization of Internal-Sn Nb$_3$Sn Composites* (Madison, WI: University of Wisconsin-Madison)

[30] Martin S, Walnsch A, Nolze G, Leineweber A, Léaux F and Scheuerlein C 2017 The crystal structure of $(Nb_{0.75}Cu_{0.25})Sn_2$ in the Cu–Nb–Sn system *Intermetallics* **80** 16–21

[31] Pong I, Oberli L-R and Bottura L 2013 Cu diffusion in Nb$_3$Sn internal tin superconductors during heat treatment *Supercond. Sci. Technol.* **26** 105002

[32] Schindelin J *et al* 2012 Fiji: an open-source platform for biological-image analysis *Nat. Methods* **9** 676–82

[33] Lee P J 2018 ASC ImageJ macros for obtaining minimum thickness measurements for layers (https://doi.org/10.5281/zenodo.1213255)

[34] Soika R, Cooley L D, Ghosh A K and Werner A 2004 Fixture for short sample testing of modern high energy physics Nb$_3$Sn strands *Advances in Cryogenic Engineering: Trans. of the Int. Cryogenic Materials Conf. (ICMC)* vol 711, pp 67–74

[35] Naus M T, Jewell M C, Lee P J and Larbalestier D C 2002 Lack of influence of the Cu–Sn mixing heat treatments on the super-conducting properties of two high-Nb, internal-Sn Nb$_3$Sn conductors *Advances in Cryogenic Engineering (ICMC)* vol 614, pp 1016–23

[36] Lyman T (ed) 1973 *Metals Handbook, Volume 8: Metallography, Structures and Phase Diagrams* 8th edn (Materials Park, OH: American Society for Metals)

[37] Motowidlo L R and Ozeryansky G M 2008 A Nb$_3$Sn conductor via Cu$_5$Sn$_4$ PIT process for high field applications *AIP Conf. Proc.* **986** 269–76

[38] Cogan S, Holmes D S and Rose R M 1979 On the elimination of Kirkendall voids in superconducting composites *Appl. Phys. Lett.* **35** 557–9

[39] McDonald W K 1981 Composite construction process and superconductor produced thereby *US Patent* US4262412 A

[40] Gregory E, Ozeryansky G M and Suenaga M 1991 Some effects of porosity and HIP'ing on critical currents in internal-tin-processed multifilamentary Nb$_3$Sn wires *CONF-9110306–1* (Upton, NY: Brookhaven National Laboratory) BNL-46846

[41] Sheth M K *et al* 2012 Study of filament cracking under uniaxial repeated loading for ITER TF strands *IEEE Trans. Appl. Supercond.* **22** 4802504

[42] Higuchi N, Tsuchiya K, Klamut C J and Suenaga M 1984 Superconducting properties of Nb$_3$Sn multifilamentary wires fabricated by internal tin process *Advances in Cryogenic Engineering Materials* ed A F Clark and R P Reed (Berlin: Springer) pp 739–46

[43] Dietderich D R, Glazer J, Lea C, Hassenzahl W V and Morris J W 1985 The critical current density and microstructural state of an internal tin multifilamentary superconducting wire *IEEE Trans. Magn.* **21** 297–300

[44] Cheggour N *et al* 2014 Influence of the heat-treatment conditions, microchemistry, and microstructure on the irreversible strain limit of a selection of Ti-doped internal-tin Nb$_3$Sn ITER wires *Supercond. Sci. Technol.* **27** 105004